

Hubble Space Telescope observations of the nucleus and inner coma of comet 19P/1904 Y2 (Borrelly)^{*}

Philippe L. Lamy¹, Imre Toth^{1,2}, and Harold A. Weaver³

¹ Laboratoire d'Astronomie Spatiale du C.N.R.S., BP 8, F-13376 Marseille Cedex 12, France

² Konkoly Observatory, Budapest H-1525, P.O. Box 67, Hungary

³ Department of Physics and Astronomy, The Johns Hopkins University, Baltimore, MD 21218, USA

Received 9 July 1997 / Accepted 22 April 1998

Abstract. The nucleus of comet 19P/Borrelly was detected using the Planetary Camera (WFPC2) of the Hubble Space Telescope (HST). During the time of our observations, the comet was 0.62 AU from the Earth, 1.40 AU from the Sun, and had a solar phase angle of 38°. The high spatial resolution of the HST images allowed us to discriminate clearly between the signal from the nucleus and that from the coma. The lightcurve of the nucleus indicates that it is a highly elongated body rotating with a synodic period of 25.0±0.5 hr. Assuming that the nucleus has a geometric albedo of 4% and is a prolate spheroid with a rotational axis pointing in the direction determined by Sekanina (1979), we derive that its semi-axes are 4.4±0.3 km and 1.8±0.15 km. The corresponding fractional active area of ~8% suggests a moderately active comet. The highly anisotropic coma is dominated by a strong sunward fan, and the dust production rate exhibited signs of temporal variability throughout our observations.

Key words: comets: individual: 19P/Borrelly – comets: general – techniques: image processing

1. Introduction

We recently demonstrated for the case of comet 4P/Faye that the high spatial resolution afforded by the HST makes it possible to discriminate between light reflected by the nucleus and light reflected by dust in the coma for comets passing reasonably close to the earth (Lamy and Toth, 1995). We now report the successful detection of the nucleus of comet 19P/Borrelly using the WFPC2, an instrument that corrects for the effects of HST's spherical aberration.

2. Observations and preliminary data analysis

The periodic comet 19P/Borrelly passed to within ~0.62 AU of the Earth in early December 1994, approximately one month

Send offprint requests to: P.L. Lamy.

^{*} Based on observations made with the NASA/ESA Hubble Space Telescope, obtained at the Space Telescope Science Institute, which is operated by the Association of Universities for Research in Astronomy, under NASA contract NAS 5-26555

after its perihelion passage on 1 November 1994. During an eleven-hour time interval on 28 November 1994, we performed six observations of the comet using the WFPC2 in Planetary Camera mode with the F675W filter, which has an effective wavelength of ~670 nm and bandwidth of 89 nm. Four images were taken during each observation: two had exposure times of 10 sec and two had exposure times of 30 sec, and all were taken within a time span of 7 mins. Table 1 lists the dates of the observations corresponding to the midpoints of the four consecutive images. The heliocentric distance (r), the geocentric distance (Δ), and the solar phase angle (α) of the comet remained practically constant during these observations at 1.401 AU, 0.622 AU, and 38°, respectively. The WFPC2 pixels are square and are 0.''0455 on a side, which projected to a distance of 20.5 km at the comet.

Our choice of the F675W filter – instead of the F702W filter used for P/Faye – was motivated by its superior photometric accuracy. As a primary WFPC2 filter, it benefits from detailed, extensive calibrations, and the conversion to standard (Landolt) R magnitudes requires only the V–R color of the object, and not both V–R and V–I, as required for the F702W filter and which introduces additional uncertainty.

All images were processed using the Routine Science Data Processing System at the Space Telescope Institute. Cosmic ray impacts were removed using a standard technique based on image duplication. Careful examination of the four images taken during each of the six visits using the x and y profiles through the pixel of maximum signal revealed no detectable shifts among them. This results from the short time spanning the sequence (7 mins) and the excellent tracking capability of HST which we have now verified on several comets. Consequently, the four images in each visit were co-added to increase the signal-to-noise ratio, giving a total effective exposure time of 80 sec. The only exception is the sixth observation, for which there was a mismatch of a fraction of a pixel between the individual images, resulting from a change of guide stars. Consequently, we separately processed the two long exposures for the sixth observation.

A comparison of the new WFPC2 images of 19P/Borrelly with the past WFPC images of comet 4P/Faye revealed impressive differences, notably the total absence of spherical aberration.

Table 1. Log of observations, photometry and size of the nucleus of comet 19P/Borrelly

Date 1994 Nov (UT)	V_{app} (mag)	$V(1,1,0)$ (mag)	$R(1,1,0)$ (mag)	R_{nucl} (km)
28.41	17.38	16.16	15.66	2.12
28.55	17.88	16.66	16.15	1.68
28.68	17.26	16.04	15.54	2.24
28.74	16.99	15.77	15.27	2.53
28.81	16.90	15.68	15.18	2.64
28.88	17.19	15.98	15.47	2.31

tion in the WFPC2 images and the strong anisotropy of the coma of 19P/Borrelly, which had a pronounced dust fan in the solar direction (Fig. 1).

The key aspect of the data analysis is to separate correctly the signal of the nucleus from that of the coma. Our previous approach of fitting an appropriate model of the comet to the images, taking into account the Point Spread Function (PSF) of the telescope, remains valid. However, its practical implementation has been radically modified to cope with the new, corrected PSF of the telescope as well as with the complex morphology of the coma of 19P/Borrelly. An accurate knowledge of the PSF is of particular importance. We used version 4.0b of the TinyTIM software written by Krist (1995). This version includes mirror zonal error maps obtained from phase retrieval of on-orbit WFPC2 data and revised aberration specifications, which significantly improve the PSF models compared to previous versions. Using this software, PSFs can be created at finer samplings than the detector pixel, a distinct advantage when dealing with the undersampled WFPC2 data and possible sub-pixel effects. All PSFs used in this study were calculated for the actual locations of the nucleus on the WFPC2 chip.

In order to assess the relative contributions of the nucleus and coma to the observed signals in the central pixels, we ran a preliminary experiment using a simple model in which the coma surface brightness decreases as ρ^{-1} , where ρ is the projected distance between the line-of-sight and the nucleus, and the light distribution from the nucleus is described by the PSF. This is the situation that should apply when there is steady-state, spherically symmetric outflow of dust from the nucleus with constant velocity. The corresponding total surface brightness distribution is given by:

$$B(\rho) = [k_c/\rho + k_n \delta(\rho)] \otimes PSF \quad (1)$$

where $\delta(\rho)$ is the Dirac δ function and \otimes is the convolution operator.

After making a crude fit of the model to a few images, we were able to reach the following conclusions:

- i) The nucleus is unambiguously detected.
- ii) The signal from the nucleus drops to insignificant levels at a cometocentric distance of ~ 100 km ($\sim 0''.22$), which

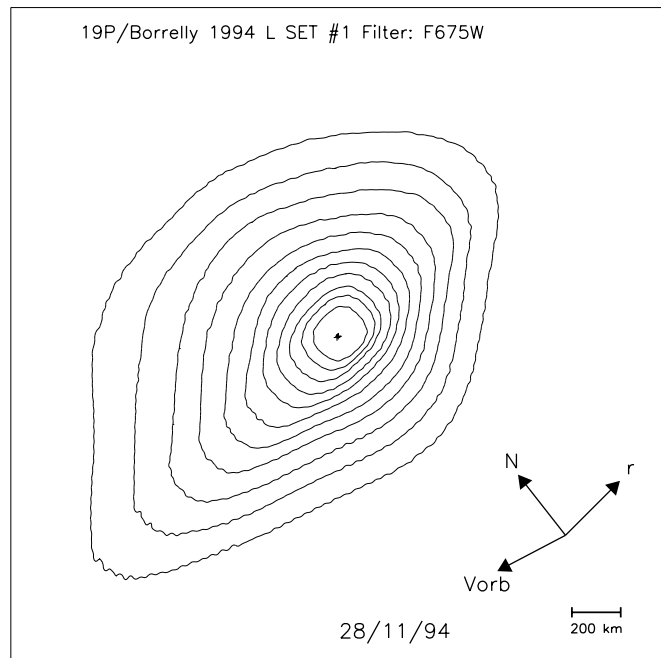


Fig. 1. Isophotal contours of the inner coma of 19P/Borrelly show an impressive dust fan in the sunward direction (isophote levels are in $\log_{10}(\text{DN})$). The arrows indicate the anti-solar direction (prolonged radius vector r), the direction of celestial north (N), and the heliocentric orbital velocity vector (V_{orb}) of the comet projected onto the sky plane.

implies that the signal beyond this point is essentially all due to the coma.

- iii) The gradient in the coma surface brightness profile (-1 in this case) is affected by the PSF only within a radius of ~ 120 km.
- iv) Sub-pixel specification of the nucleus significantly improves the fit of the model to the data.
- v) This simple model obviously does not provide an adequate description of the highly anisotropic coma of 19P/Borrelly.

3. The coma model

Given the shortcomings described above, we developed an improved model, which we now describe in detail. The first step is to construct an anisotropic model of the coma using the observed spatial brightness profiles. The noise in the outer part of the coma, where the observed signal became weaker, was reduced by applying an inverse gradient filter, which preserves the slope of the brightness distribution. We then performed a polar transform of the images centered on the nucleus (the pixel having the largest signal) with an angular resolution of 1° (i.e., 360 profiles were created). Each of the 360 lines in the polar image may be represented by a power law $B_i(\rho) = A_i \rho^{p_i}$, $i \in [1, 360^\circ]$. The 2×360 parameters, A_i and p_i , were determined by least-squares fits to the observed profiles in a restricted interval that contained “uncontaminated” coma. Specifically, we used the region defined by $140 \leq \rho \leq 600$ km to fit the coma parameters, as the contribution to the signal by the nucleus was negligible there and the gradient was essentially unaffected by convolution with

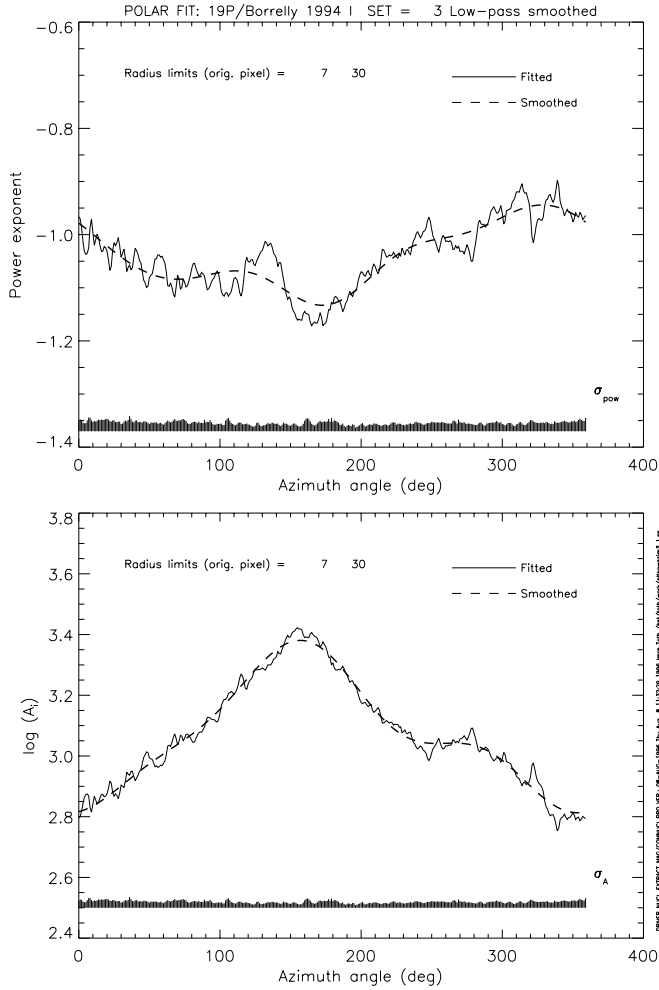


Fig. 2. The angular variations of the parameters $p_i(\Theta)$ (top) and $A_i(\Theta)$ (bottom) for the third observation are plotted. The residuals from the fit (stick plots) and the adopted smoothed values for the parameters are also displayed (dashed-line).

the PSF. Fig. 2 shows an example of the angular variations of $A_i(\Theta)$ and $p_i(\Theta)$ and illustrates both the strong anisotropy of the coma and the clear deviation from the canonical law $p = -1$. We note that the fit to the coma is excellent, as indicated by the small residuals displayed in the figure.

The full coma model is now constructed assuming that the above parametric representation holds also for $\rho < 140$ km. Small-scale variations in the fitted parameters were filtered out (see Fig. 2), as they may be artifacts of our coordinate transformation and, in any case, are irrelevant for determining the size of the nucleus. The model images of the coma were generated on an 8 times finer grid than the original WFPC2 pixel. At this new scale, in which the sub-pixel projects to a linear distance at the comet of ~ 2.6 km, the effect of the finite size of the nucleus can be introduced. Our preliminary analysis of Sect. 2 indicated that the nucleus had an effective radius of 2.5 km, so we assumed that a 2×2 sub-pixel region defined the location of the nucleus. For all pixels other than the ones containing the nucleus, polar coordinates were computed from the cartesian coordinates and

the appropriate parametric laws were used to calculate the coma signal in each sub-pixel. The four sub-pixels containing the nucleus were not set to zero but to one-half the average value of the surrounding pixels, since half the line-of-sight is blocked by the nucleus. While the actual coma contribution to the sub-pixels containing the nucleus may differ somewhat from our prescription, the derived nuclear magnitude is only weakly dependent on the exact choice because the sub-pixels are so much smaller than the actual WFPC2 pixel (i.e., there is a significant dilution effect). Furthermore, convolution with the PSF washes out fine details, as illustrated in Fig. 3. We note that the center of the nucleus does not necessarily coincide with the opto-center of the coma, as expected for an anisotropic coma. This effect was dramatically illustrated in the high resolution images of comet 1P/Halley obtained by the GIOTTO/HMC camera (Keller et al. 1994); in both cases (1P/Halley and 19P/Borrelly) the brightness distribution is skewed in the solar direction due to the enhanced dust emission from the sub-solar region.

Finally, each coma model was convolved with a PSF that was also sampled on the finer grid, using the TinyTIM software discussed in Sect. 2.

4. The retrieval of the nucleus

A complete model image of the comet is obtained by superimposing the nucleus on the coma model described above. The nucleus is represented by the scaled point spread function, $k_n PSF$. In order to make a comparison with the observed images, the model image must be integrated over the 8×8 sub-pixels to recover the original pixel of the WFPC2. In performing this integration, we allowed for 64 different possibilities, corresponding to the 64 possible locations of the nucleus (x_n, y_n) on the sub-sampled grid. The location of the nucleus and the scaling factor k_n were determined by minimizing the residuals $Q(x_n, y_n, k_n)$ between the model and observed images:

$$Q(x_n, y_n, k_n) = \left| \int \int [k_n PSF + comamodel \otimes PSF] dx dy - data \right| \quad (2)$$

Note that the magnitude of the coma is not a free parameter, as that was fixed by the fitting procedure used to derive the coma model. The location of the nucleus is apparently located very accurately, as illustrated in Fig. 4, which displays the x profiles for the optimum value of y_n and the y profiles for the optimum value of x_n . A non-optimal value of k_n was used to increase the clarity in the plot but the best solution is obviously that which closely parallels the observed profiles.

The 1σ noise of a signal B is given by

$$s = \sqrt{\frac{B}{g} + \left(\frac{\mathfrak{R}}{g}\right)^2 + (fB)^2} \quad (3)$$

where $g = 7$ electrons/DN is the gain, $\mathfrak{R} = 5$ electrons is the readout noise, and $f = 0.01$ expresses the flat field noise as a fraction of the signal. For a typical signal of 2000 DN, the 1σ value of the noise is 26 DN, which is insignificant compared

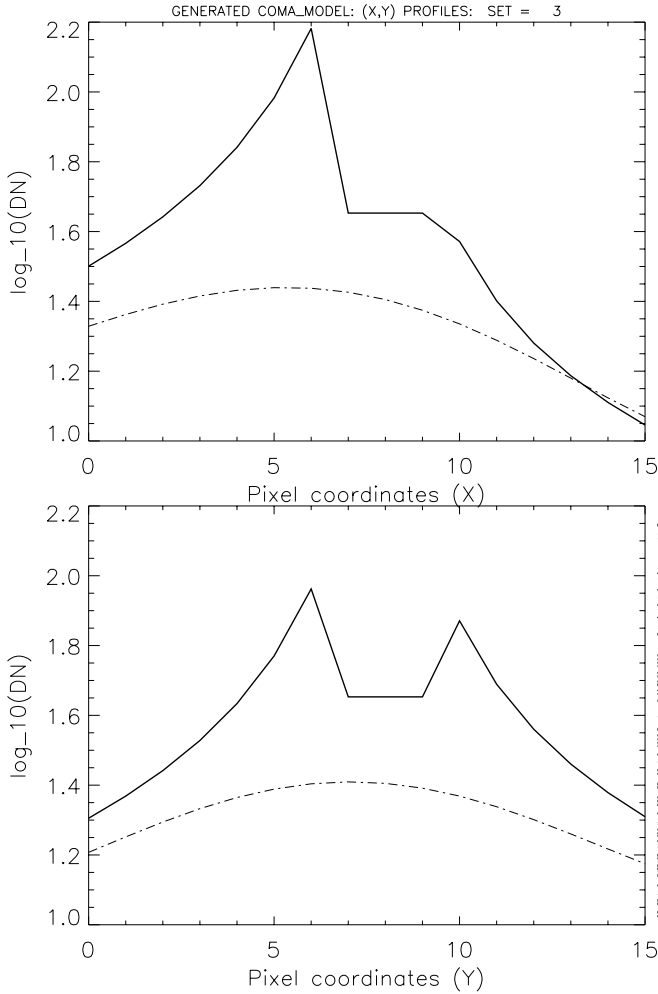


Fig. 3. Profiles of the coma model generated on the resampled grid before (solid line) and after (dashed-line) convolution with the PSF. This case corresponds to the third observation.

to the differences between the models and the data plotted in Fig. 4. Although our procedure provides excellent discrimination among different sub-pixel locations of the nucleus, we note that our determination of the nuclear magnitude is essentially unaffected by the exact location. The primary benefit of including sub-pixel sampling is to improve the fit between the model and the data (i.e., sub-sampling allows a better approximation to the skewness of the spatial brightness distribution).

An example of the results from our minimization procedure is displayed in Fig. 5, where the residual Q is plotted as a function of the three parameters x_n , y_n and k_n . $Q(k_n)$, shown for the optimum values of the coordinates, is very well behaved and allows a precise determination of k_n .

Fig. 6 illustrates the details of our solution for the third observation. The different skewness of the x -profiles of the coma and the nucleus is readily explained by the fact that the nucleus is not located at the opto-center of the coma, as already discussed. As expected, the detailed variations of the coma signal illustrated in Fig. 3 are washed out by the convolution with the PSF and by the integration over the original pixel. In prac-

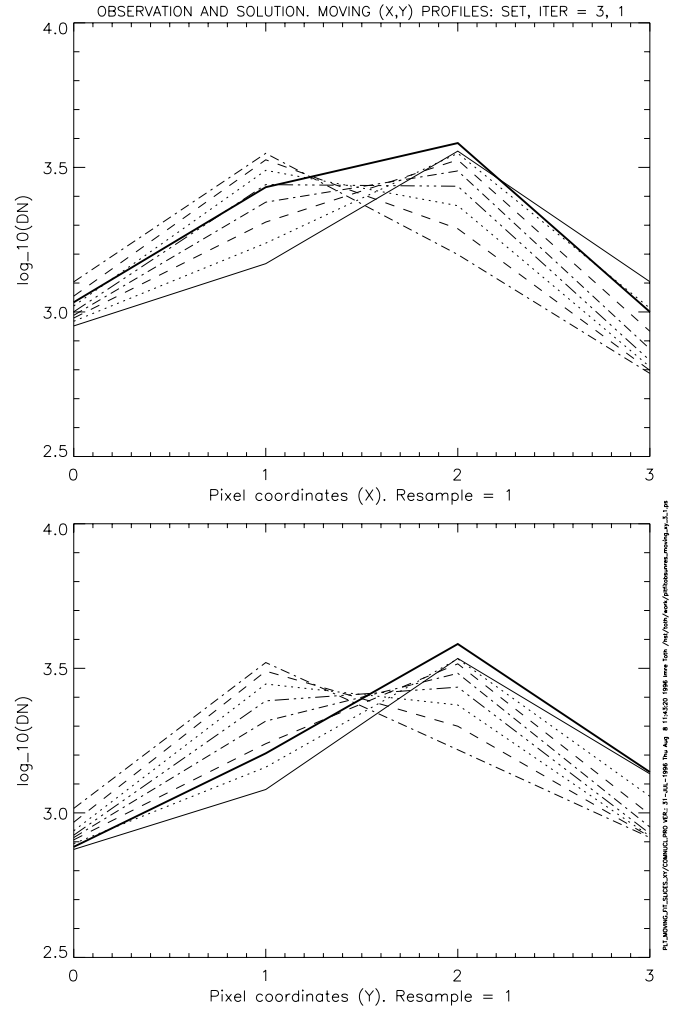


Fig. 4. Influence of the sub-pixel location of the nucleus: comparison of a family of solutions with the observation (thick solid line).

tice, the coma model is rather insensitive to sub-pixel brightness variations, as checked by several tests.

Fig. 7 compares the model comet with the observed image on an expanded vertical scale. Although the quality of the fit looks excellent, one must remember that the plot has a logarithmic scale. In reality, the deviations between the model and the data in the core of the image are significantly larger than what would be expected based on photon-dominated noise statistics. We suspect that the large deviations are caused by our inability to represent accurately the highly anisotropic coma of 19P/Borrelly, as our residuals are significantly smaller for comets having a more circularly symmetric surface brightness distribution. In any case, the residuals from our fits are still less than 10% of the observed peak intensities, indicating that our retrieved size for the nucleus is not significantly affected by the imperfect fitting.

Absolute magnitudes for the nucleus were determined from the scaled PSFs that best matched the observations (i.e., the k_n PSF distributions, which represent the nucleus as it would be observed by the HST in the absence of coma). Following Holtzman et al. (1995), we calculated instrumental magnitudes

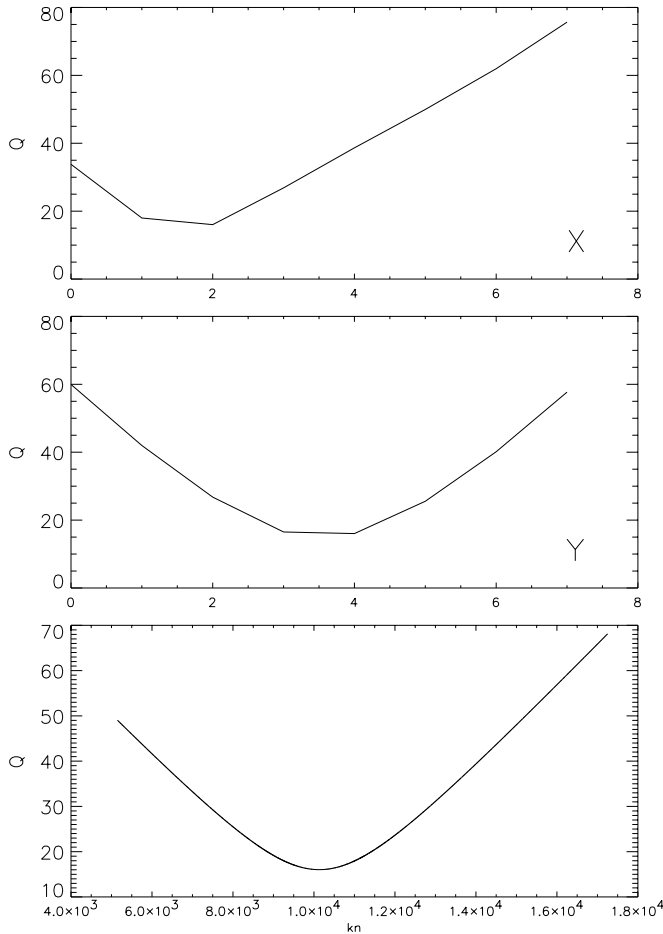


Fig. 5. Variations of the residual Q with x_n (top), y_n (middle), and k_n (bottom).

by integrating the scaled PSFs over an aperture having a radius of $0.''5$, so that no aperture correction is required. We did not apply a correction for the charge transfer efficiency, since the coma ensured that there was a large background signal. Nor did we make any correction for observing geometry, as the nucleus was always located near the center of the CCD. The conversion to standard (Landolt) R magnitudes, and the additional transfer to V magnitudes, required knowledge of the V–R colour of the nucleus. As we did for comet 4P/Faye, we used $V-R = 0.505$, which corresponds to an “average” reddening of 17% per 10^3 \AA (Jewitt, 1992). The so-called reduced magnitudes $V(1,1,0)$ and $R(1,1,0)$, which refer to the standard conditions $r = \Delta = 1 \text{ AU}$ and $\alpha = 0^\circ$, were calculated assuming a linear variation of the phase function of the nucleus with the phase angle (using a coefficient of 0.04 mag/deg). These results are given in Table 1. In order to compare them with the photographic magnitudes of the “nucleus condensation” (Roemer, 1965), we first applied a standard correction of -0.8 mag to convert from photographic to V magnitudes and the above phase law to obtain reduced magnitudes. These corrected values are scattered between 15 and 13, which are well outside our range. The faintest value of 15 was obtained when the comet was at

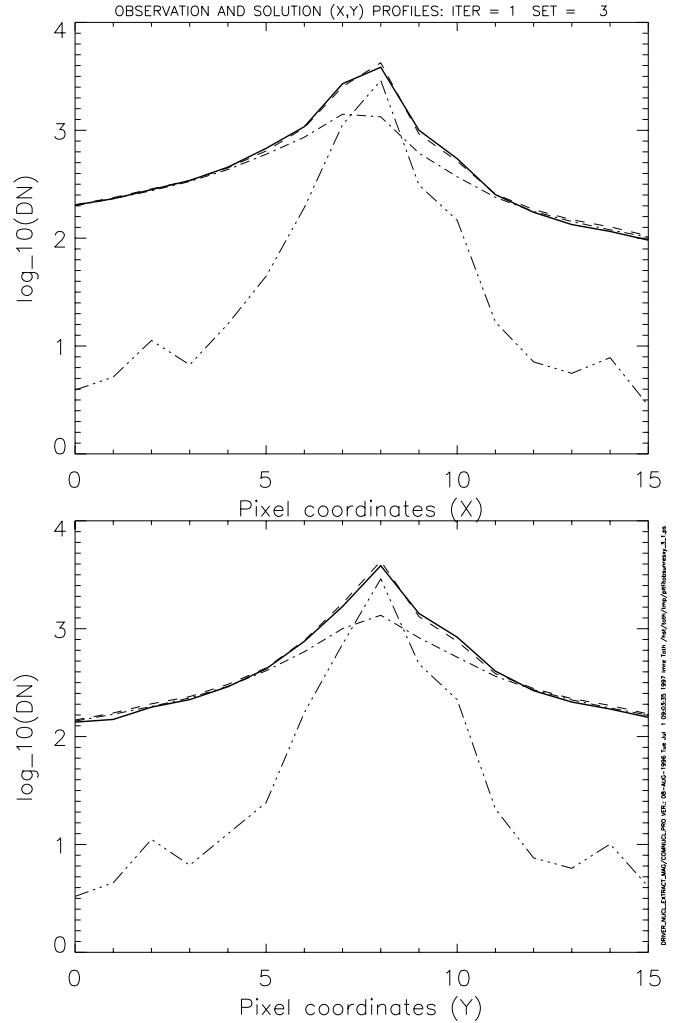


Fig. 6. Comparison of the third observation (thick solid line) with the coma model (dash line), the nucleus model (dash-triple-dot line) and the coma + nucleus model (dash-dot line).

3.5 AU and is approximately 0.7 mag brighter than our brightest value, suggesting the plausible persistence of a coma even at this large heliocentric distance. Our range of apparent nuclear magnitudes ($\sim 1 \text{ mag}$) is comparable to that of comet 1P/Halley, but substantially larger than that of other comets (Jewitt, 1992).

5. Discussion of errors

As mentioned in Sect. 2, the two images of the sixth observation were processed separately because they differed in the sub-pixel location of the nucleus. We find that the magnitudes derived from these two images differ by only 0.01 mag, which lends further credibility to our technique.

The uncertainties in the coefficients involved in the transformation of the instrumental to absolute magnitudes (zero-points, color coefficients) lead to an error of 0.014 mag.

The model PSF generated by the TinyTIM software is a potential source of error, as it does not exactly represent the actual PSF of the telescope. One point of particular concern

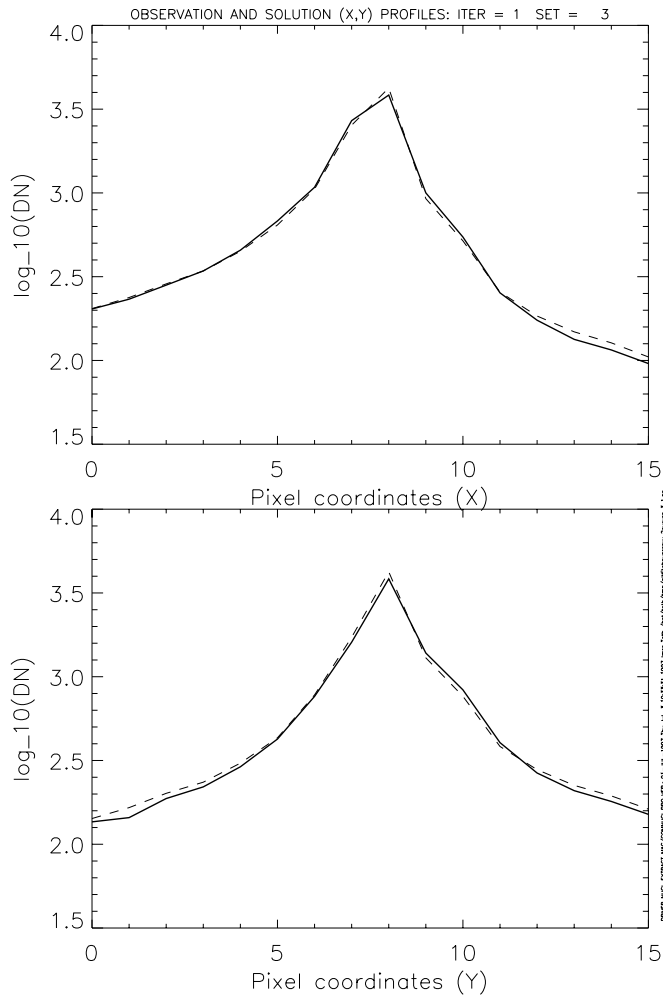


Fig. 7. Comparison of the third observation (thick solid line) with the coma + nucleus model (dash line). For signals larger than ~ 300 DN, the 1-sigma error bar is within the width of the thick solid line. See the text for further discussion.

is the jitter of the spacecraft, which is not known when the telescope is tracking a moving target. A direct measure of the jitter could be determined by analyzing star trails, but there were no bright stars in the 19P/Borrelly field. However, variable amounts of jitter can be introduced in the TinyTIM calculation in order to estimate its effect. In essence, the jitter makes the PSF slightly “fatter”, thus decreasing the contribution of the coma in the central pixels and making the nucleus brighter. The jitter is usually characterized by the rms value of the fluctuations of the pointing direction in milliarcsec (mas). A reasonable estimate of 10 mas led to a brightening of the nucleus by 0.014 mag while an extreme value of 20 mas increased the nuclear magnitude by 0.047 mag.

Scattering of light by the CCD electrodes has an effect on the PSF that is similar to that produced by jitter, so we do not consider that effect separately here.

In summary, we adopt a conservative value of ± 0.05 mag for the error in the nuclear magnitudes due to the effects discussed above.

Turning now to the systematic errors, we first discuss our key assumption that the gradients of the coma can be extrapolated within 140 km of the nucleus. The only data relevant to this issue are the high resolution images of 1P/Halley obtained by the Giotto/HMC camera. Analyses of those images indicate that the spatial brightness profile has a constant gradient between 200 and 600 km - very much like what we found for 19P/Borrelly - and a conspicuous flattening inside 200 km, which is possibly explained by the fragmentation of dust grains in the coma (Thomas and Keller, 1990; Keller, Marconi, and Thomas, 1990). Note that this latter effect is small; for example, the intensity at a radial distance of 20 km is depressed by only $\sim 12\%$ compared to that predicted by the constant gradient model. In order to estimate the effect on our photometry of 19P/Borrelly’s nucleus, we generated flattened coma models by introducing a “flattening” function derived from the 1P/Halley profiles (Figs. 1 and 2 of Thomas et al., 1988). The contribution of the coma in the central pixels was consequently reduced, resulting in a brightening of the nucleus by 0.25 mag.

Our adopted reddening of $17\%/10^3 \text{ \AA}$ is another potential source of systematic error. Using a value of $11\%/10^3 \text{ \AA}$, as observed for P/Encke (Luu and Jewitt, 1990), decreases the R magnitude by 0.007 and the V magnitude by 0.06.

Another source of systematic error is the unknown phase law for the nucleus. Our adopted phase coefficient of 0.04 mag/deg is consistent with that estimated for some other cometary nuclei. Using a coefficient of 0.034 mag/deg, as found for P/Neujmin 1 (Jewitt and Meech, 1987), makes the nucleus fainter by 0.23 mag.

As expected, the error in the determination of the magnitude of the nucleus is dominated by systematic effects. However, these errors do not affect our results on the *relative* brightness variations of the nucleus.

6. Properties of the nucleus

The geometric cross-section of the nucleus may be calculated from $V(1,1,0)$ using a standard relation (c.f., Keller, 1990; Jewitt, 1992) and assuming a geometric albedo of 4%. From the equivalent circular cross-section, an effective radius can be computed (Table 1). The uncertainty of ± 0.05 mag translates into an uncertainty of 2.3% in the size of the nucleus, while a brightening of the nucleus of 0.25 mag, for example, increases the radius by 12%. Using an albedo of only 3.5% would increase the radius by 7%.

The above derivation assumes that the nucleus is spherical, which is clearly contradicted by the observed lightcurve (Fig. 8). The observations strongly suggest that we are seeing the apparent cross-section of a rotating elongated nucleus. In principle, albedo variations on the nucleus could produce the observed lightcurve variations, but this hypothesis is contradicted by the simultaneous visible and infrared observations of several cometary nuclei (c.f., Millis et al., 1988). We searched for periodicity in the lightcurve by constructing a Fourier decomposition limited to the first sine and cosine terms due to the limited number of data points. The coefficients of these two terms were first

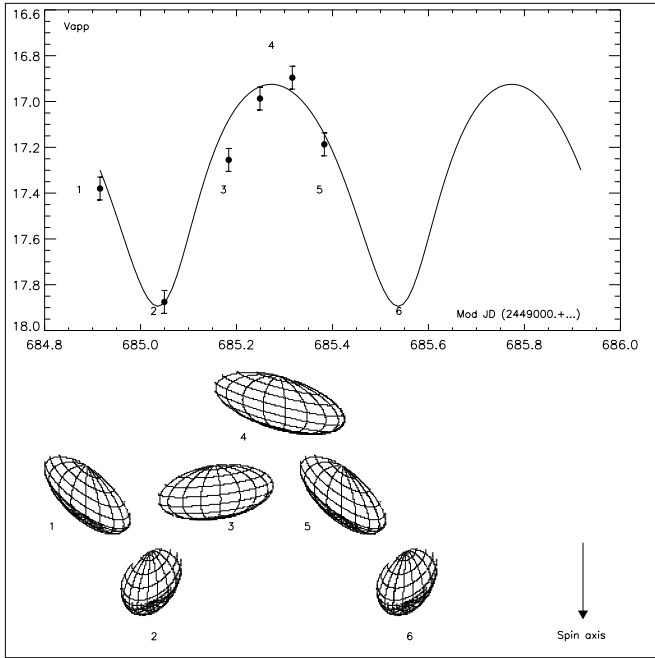


Fig. 8. Temporal variation of the brightness of the nucleus of comet 19P/Borrelly. The (Landolt) apparent V (dots) observed magnitudes are plotted versus time (modified Julian Dates: JD 2449000+...). The simulated lightcurve for the model of a rotating prolate spheroidal nucleus is plotted. Effective cross-sections as seen from Earth are displayed with the limb and shadowed regions for the six points of the lightcurve.

found using a gradient method, and the period was searched in the interval from 5 to 40 hr. A least-square fit to the data yielded $P=25$ hr. This value was then introduced as the initial guess in a full, non-linear parameter fit, which produced the same value for the period $P=25.02 \pm 0.5$ hr, as well as an accurate determination of the Fourier coefficients.

In order to reconstruct the shape of the nucleus, we assumed that it was a prolate spheroid with semi-axes a and b , that it was in rotation around one of the minor axes, and that its brightness was proportional to its geometric cross-section (the so-called geometric scattering law). Under these assumptions, the amplitude of the lightcurve becomes a function of the aspect angle ξ and the ratio a/b . The aspect angle was calculated adopting the orientation of the spin axis found by Sekanina (1979). The ecliptic longitude and latitude of the north pole are 60° and -57° , respectively (for 1950.0), implying a retrograde rotation. The viewing geometry on 28 November 1994 resulted in an aspect angle of 89° (“equatorial view”), with the spin axis being practically perpendicular to the line-of-sight. After imposing a rotational period of 25.02 hr, we find that the best fit synthetic lightcurve (Fig. 8) gives a ratio $a/b = 2.46 \pm 0.15$.

The viewing conditions of the nucleus, depicted in Fig. 8, were such that nearly the full cross-section was seen at the maximum of the lightcurve. We calculated the fraction of illuminated area (0.95) and introduced this correction to derive the true elliptic cross section πab assuming a geometric albedo of 4%. We obtained $a = 4.4 \pm 0.3$ km and $b = 1.8 \pm 0.15$ km. The errors are

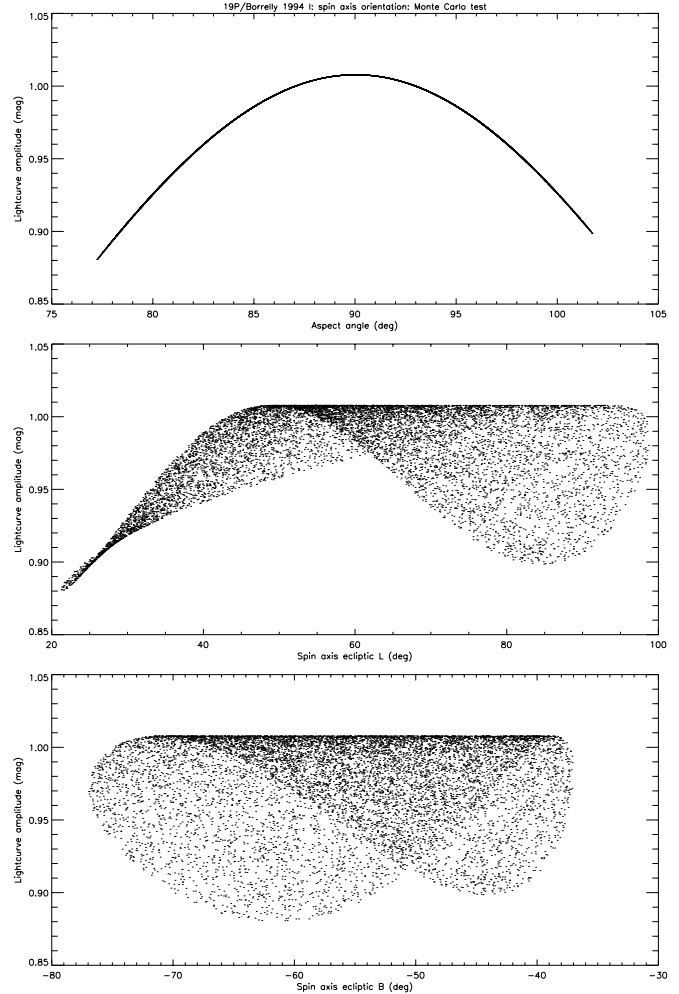


Fig. 9. Influence of the direction of the spin axis on the lightcurve: its amplitude is plotted as a function of the aspect angle (top), the ecliptic longitude (middle) and latitude (bottom) of the spin axis.

derived from the propagation of the photometric uncertainties within the framework of the above model.

We tested other solutions for the orientation of the spin axis by randomly selecting any direction within 20° of the direction found by Sekanina. Any deviation from this nominal solution, for which the aspect angle is at a maximum, results in a decrease of the amplitude of the light curve as illustrated in Fig. 9. The uncertainty in the observed lightcurve amplitude translates into a wide range of solutions for the ecliptic longitude and latitude of the spin axis, typically $\pm 30^\circ$. Similarly indeterminate solutions are well-known in the study of asteroidal lightcurves having limited data, as applies to our case also.

From an analysis of the non-gravitational forces on the nucleus of 19P/Borrelly, Rickman et al. (1987) derived that the mass of the nucleus is 8.2×10^{12} kg. Combining the latter with our result on the shape of the nucleus leads to a bulk density of ~ 140 kg m $^{-3}$, a somewhat low value but still within the range of presently accepted values. The nucleus of 19P/Borrelly is stable against centripetal disruption since the critical density (Jewitt and Meech, 1988) is much lower, $\rho_c = 45$ kg m $^{-3}$. Fi-

nally, from the active area of 6.6 km^2 obtained by A'Hearn et al. (1995), and the total area of the equivalent spheroidal nucleus, we calculated a fractional active area of 8 %, comparable to that of comet 1P/Halley (10 %).

7. Properties of the coma

7.1. Calibration of the surface brightness

Holtzman et al. (1995) gives the physical zeropoint of the WFPC2 magnitude system for an object having a Vega-type spectrum with $m = 0$ and observed through the F675W filter: $F_0 = 2.021 \times 10^{-9} \text{ erg sec}^{-1} \text{ cm}^{-2} \text{ \AA}^{-1}$. Their Eq. 7 allows one to relate the WFPC2 magnitude to the observed signal S in DN sec^{-1} :

$$WFPC2 = -2.5 \log S + Z_{WFPC2} + 2.5 \log GR_i \quad (4)$$

where $GR_i = 1.987$ and $Z_{WFPC2} = 21.234$ is the zeropoint for the F675W filter. As recommended, we added 0.1 mag to the zeropoint to correct to an infinite aperture. The flux expression:

$$F = F_0 10^{-0.4WFPC2} \quad (5)$$

can now be rewritten as:

$$F = 2.977 \times 10^{-18} S \text{ erg sec}^{-1} \text{ cm}^{-2} \text{ \AA}^{-1} \quad (6)$$

The standard flux calibration factor given by the routine processing (FITS keyword “PHOTFLAM” in the image header), which strictly applies to a source with a constant flux per unit wavelength, has been revised in version 2 (December 1995) of the HST Data Handbook to 2.8×10^{-18} . The agreement between the two derivations is excellent (3.4 %) and, as expected, the calibration factor is practically independent of the spectral type.

The final calibration formula, which relates the pixel value S (DN sec^{-1}) to the absolute surface brightness B in $\text{W cm}^{-2} \text{ sterad}^{-1} \mu\text{m}^{-1}$, involves the solid angle subtended by a pixel of the WFPC2 ($\Omega = 4.866 \times 10^{-14} \text{ sterad}$) and is given by:

$$B = 6.118 \times 10^{-8} S \quad (7)$$

Based on the previous discussion, the uncertainty is $\sim 4 \%$.

7.2. The radial gradients

Fig. 10 displays the radial surface brightness profiles of the coma averaged over four sectors having 30° angular extents and centered, respectively, along the solar and anti-solar directions and in the perpendicular directions (the latter almost correspond to the North–South direction; see Fig. 1). The power law exponents of these average profiles are practically constant from $\rho = 150$ to 1000 km but deviate somewhat from the canonical $p = -1$ value. The largest deviation occurs for the solar sector, where p ranges from -1.08 (5th and 6th observations) to -0.96 (1st and 2nd observations) with an intermediate value of -1.02 for the 3rd and 4th observations. The situation is much simpler in

the anti-solar direction, where the six profiles exhibit nearly the same gradient of -0.97 except for some slight variations inside 160 km. The north and south sectors display intermediate situations; note that beyond ~ 400 km all the profiles converge but with distinct gradients, -1.03 (north) and -1.07 (south). While these average profiles allow a gross characterization of the inner coma of 19P/Borrelly, they tend to hide a more complex reality, which is best revealed by the angular variations of the parameters A_i and p_i introduced in Sect. 2 (Fig. 11). There is a gross anti-correlation between the two parameters as p_i tends to reach its minimum value when A_i reaches its maximum value. The first and, to a lesser extent, the second observations are somewhat at odds with this trend. The broad fan is systematically offset from the solar direction by approximately 20° , except for the first observation where there is no offset. Note that the minima of p_i are further offset, by approximately 40° . A secondary maximum, or shoulder, is clearly present at about 40° from the antisolar direction. The power exponent, p_i , is close to its canonical value only in a sector close to the antisolar direction where the amplitudes A_i roughly reach their minimum value.

7.3. Temporal variations

Fig. 11 indicates that the largest temporal variation of the brightness of the coma takes place in the sunward fan and reaches a factor ~ 2 , which roughly corresponds to the variation of the cross-section of the nucleus illuminated by the Sun. (If the aspect angle is close to 90° as discussed above, the Sun sees a cross-section almost identical to that seen by the Earth as illustrated in Fig. 8, with a time lag of 2.6 hr corresponding to the solar phase angle of 38°). However, the situation is more complex as the variation of the maximum value of A_i does not strictly follow the nuclear lightcurve, especially for the first and second observations. Nevertheless, the emission pattern of dust is clearly determined by the insolation of the sub-solar region of the nucleus.

7.4. $Af\rho$ and the dust production rate

Although the quantity $Af\rho$, as introduced by A'Hearn et al., (1984) is not strictly applicable to a coma that is not in steady-state, we calculated it for 19P/Borrelly to allow a comparison with ground-based measurements. We first subtracted the contribution of the nucleus, and then integrated the coma signal using an aperture radius of 2400 km ($5''.3$). The results for the six observations fall in the range 600–620 cm and compare very favorably with the value of 646 cm obtained by A'Hearn et al. (1995) when the comet was at a mean heliocentric distance of 1.38 AU (i.e., slightly closer to the Sun than for the present observations).

The determination of the dust production rate follows exactly the method we used for comet 4P/Faye (Lamy et al., 1996), except that the required parameters were set to the values appropriate for 19P/Borrelly: an effective radius of 2.4 km, a fractional active area of 8 % (derived above), and an OH production rate of $1.86 \times 10^{28} \text{ molecules sec}^{-1}$. The

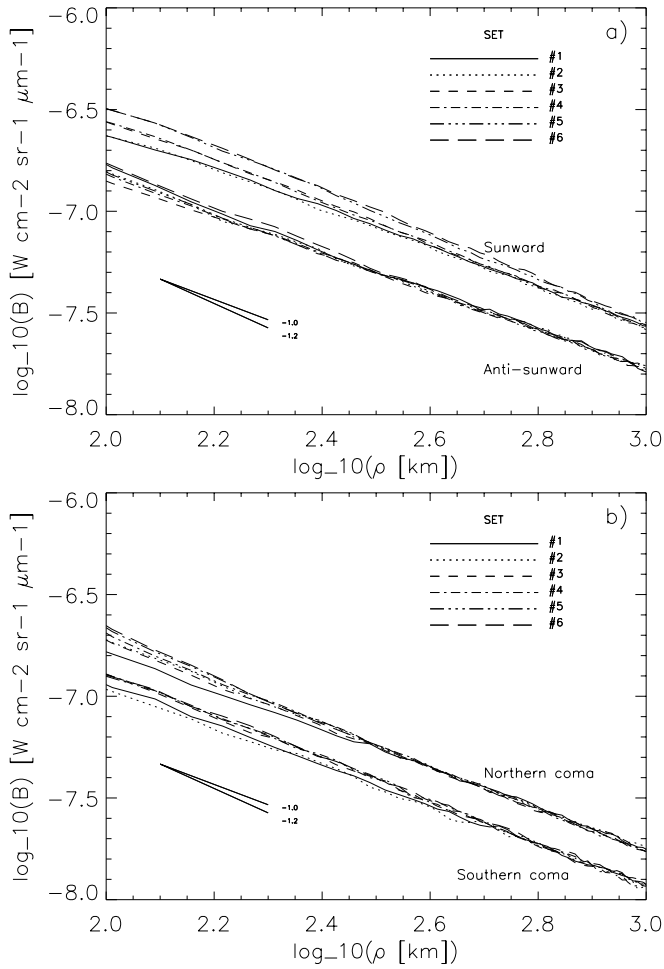


Fig. 10. The average brightness profiles of the coma of comet 19P/Borrelly in the solar and antisolar directions (top) and in the North and South directions (bottom)

latter value was measured by A’Hearn et al. (1995) at a heliocentric distance of 1.41 AU, which is sufficiently close to the present value (1.401 AU) that no correction is required. We assumed that the gas production was dominated by water with $Q_{H_2O} = 1.1 \times Q_{OH} = 2.05 \times 10^{28}$ molecules sec^{-1} . We calculated the dust production rate for two values of the bulk density of the nucleus, the canonical value of 1000 kg m^{-3} and 140 kg m^{-3} , the value derived above using previous results from a non-gravitational force analysis, and obtained 180 and 215 kg sec^{-1} , respectively. We calculated dust production rates using three different aperture sizes (500, 1000, and 2400 km) and found essentially no difference among them. During the 1981 apparition, at a heliocentric distance of ~ 1.34 AU, Newburn and Spinrad (1989) estimated a dust production rate of about 335 kg sec^{-1} , assuming a nuclear radius of 3.5 km and an active fraction of 10%. During the 1987 apparition at a heliocentric distance of ~ 1.5 AU, Singh et al. (1992) obtained 240 kg sec^{-1} assuming a radius of 4 km and a similar active fraction. In view of the large errors inherent in the method (a

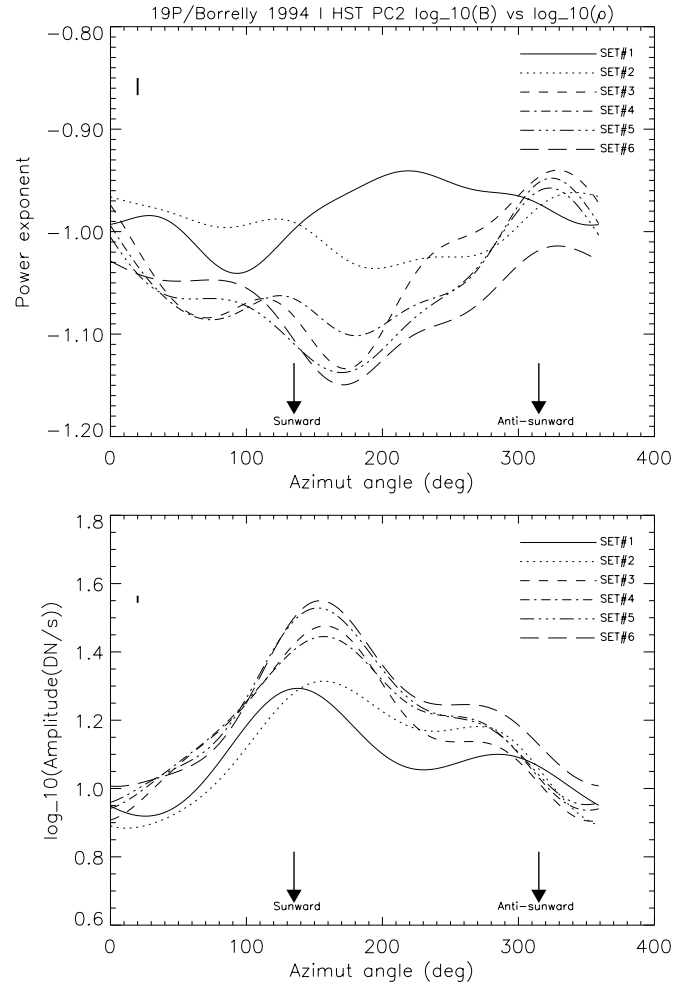


Fig. 11. The angular variations of the parameters $p_i(\Theta)$ (top) and $A_i(\Theta)$ (bottom) for the six observations.

factor 2 error is estimated by Newburn and Spinrad, 1985), we conclude that these values are in reasonable agreement.

8. Conclusions

The unambiguous detection of the nucleus of comet 19P/Borrelly with the Hubble Space Telescope reveals a highly elongated body with semi-axes of $a = 4.4 \pm 0.3$ km and $b = 1.8 \pm 0.15$ km (yielding $a/b = 2.46 \pm 0.15$), and rotating with a synodic period of $25. \pm 0.5$ hr. Our interpretation of the observed lightcurve as resulting from the rotation of a prolate spheroid gives an orientation of the spin axis consistent with that derived by Sekanina (1979); however, the constraints on the orientation are not very strong. Although the size of 19P/Borrelly’s nucleus is approximately half that of comet 1P/Halley, the rotational period of 25 hr and the fractional active area of 8% suggest some similarity between the two nuclei: both are more active and probably less evolved than the majority of the short-period comets. Comet 19P/Borrelly exhibits a complex coma dominated by a strong dust fan in the solar direction. We are

presently investigating its detailed morphology to determine the pattern of active areas on the nucleus.

Acknowledgements. We express our gratitude to A. Storrs of the Space Telescope Science Institute for masterly scheduling our time-critical observations so as to properly sample the lightcurve, to A. Llebaria of LAS for enlightening discussions on image processing, to G. Schwarz of DLR for providing specific software, and to M. A'Hearn for reviewing the manuscript. This work was supported by grants from the Université de Provence and from the "Action de Soutien Télescope Spatial".

References

- A'Hearn, M.F., Schleicher, D.G., Feldman, P.D., Millis, R.L., and Thompson, D.T., 1984, *AJ* 89, 579
- A'Hearn, M.F., Millis, R.L., Schleicher, D.G., Osip, D.J., and Birch, P.V. 1995, *Icarus* 118, 223
- Holtzman, J.A. et al. 1995, *PASP* 107, 1065
- Jewitt, D.C., and Meech, K.J. 1988, *ApJ* 328, 974
- Jewitt, D., 1992, in Proc. 30th Liège Internat. Astrophys. Colloq., Inst. d'Astrophys., Univ. Liège, A. Brahic, J.-C. Gerard, & J. Surdej Eds., Univ. of Liège Press, Liège, p. 85
- Keller, H.U., 1990, in *Physics and Chemistry of Comets*. W.F. Huebner Ed., Springer-Verlag, Berlin, p. 13
- Keller, H.U., Marconi, M.L., Thomas, N., 1990, *A&A* 227, L1
- Keller, H.U., Curdt, W., Kramm, J.R., Thomas, N., 1994, in *Images of the Nucleus of Comet Halley*, R. Reinhard, N. Longdon, B. Battrick Eds., ESA SP-1127, Vol.1
- Krist, J., 1995, *ASP Conference Series Vol. 77*, R.A. Shaw, H.E. Payne, J.J.E. Hayes Eds., p. 349
- Lamy, P.L., and Toth, I. 1995, *A&A* 293, L43
- Luu, J.X. and Jewitt, D.C., 1990, *Icarus* 86, 69
- Millis, R.L., A'Hearn, M.F., and Campins, H. 1988, *ApJ* 324, 1194
- Newburn, R.L., Jr. and Spinrad, H., 1985, *AJ* 90, 2591
- Newburn, R.L., Jr. and Spinrad, H., 1989, *AJ* 97, 552
- Rickman, H., Kamél, L., Festou, M.C., Froeschlé, C., 1987, in *Symposium on the Diversity and Similarity of Comets*, E.J. Rolfe, B. Battrick Eds., ESA SP-278, p. 471
- Roemer, E. 1965, *AJ* 70, 397
- Sekanina, Z., 1979, *Icarus* 37, 420
- Singh, P.D., De Almeida, A.A., and Huebner, W.F. 1992. *AJ* 104, 848
- Thomas, N., Boice, D.C., Huebner, W.F., and Keller, H.U. 1988, *Nature* 332, 51
- Thomas, N., and Keller, H.U., 1990, *Annales Geophysicae* 8, 147